

TABLE OF CONTENTS

Section	Page
1 BEAMLINE OPTICS AND FALSE ASYMMETRIES	1
1.1 Detector Sensitivities	1
1.2 Beamline Optics	4
1.2.1 BPM Sign Corrections	7
1.2.2 Beam Modulation Tune Parameter Scan	8
1.2.3 Effect of Fast Feed Back on Beam Modulation	9
1.3 QTOR Fringe Field and Optics Change	11
1.3.1 QTOR Corrector Magnet	13
1.4 BPM Resolution	16
1.4.1 Position Resolution	16
1.4.2 Target BPM Angle Resolution	18
1.4.3 Consistency Check of the Target Variable	19
1.5 Helicity Correlated Pedestal Analysis	19
1.5.1 Motivation	20
1.5.2 Analysis Procedure and Goal	20
1.5.3 Experimental Method	21
1.5.4 Results	22
1.5.4.1 Helicity Correlated Pedestal Signal Pickup	23
1.5.4.2 Helicity Correlated Pedestal Sensitivities	24
1.5.4.3 Stability of Pedestal Subtracted Signal	25
1.5.4.4 Detector Resolution	26
1.5.5 Summary of Helicity Correlated Pedestal Survey	27
REFERENCES	29

SECTION 1

BEAMLINE OPTICS AND FALSE ASYMMETRIES

1.1 Detector Sensitivities

As described in the previous chapter, unwanted helicity correlated changes in the transverse beam positions X (horizontal) and Y (vertical), beam angles X' and Y', and incident energy E on the target give rise to false asymmetries. These helicity correlated beam asymmetries $A_{false}(X, Y, X', Y', E)$ can be heavily suppressed with careful tuning at the polarized source and a symmetric detector array. However, the residual effects must be measured and controlled. The regressed asymmetry can be expressed using the following expression:

$$\begin{aligned} A_{reg} &= A_{msr} - A_{false}, \\ A_{false} &= \sum_{i=1}^5 \left(\frac{\partial A}{\partial T_i} \right) \Delta T_i \end{aligned} \quad (1.1.1)$$

Here, the slopes $\partial A / \partial T_i$ are the measured main detector sensitivities of the asymmetry A_{raw} defined in Equation 1.1.1 to changes in the beam parameters ΔT_i at the helicity quartet level, and ΔT_i is the helicity correlated (HC) difference of each beam parameter ΔT_i measured at the quartet level. The virtual target BPM, described in section ??, was used to continuously measure the HC beam position and angle differences at the target. The measurement of the HC energy difference relied on BPM3C12, as described in Equation ?? of section ???. The natural jitter of the beam was used to determine the detector sensitivities, $\partial A / \partial T_i$. However, a better decoupling of the 5 sensitivities was achieved by varying the beam parameters in a controlled manner using a beam modulation system built specifically for this purpose. Relatively decoupled position and angle motions were separately produced by varying the current in pairs of air-core magnets placed along the beamline; two pairs in X and two pairs in Y, approximately 82 and 93 m upstream of the target.

A typical detector sensitivity for X modulation during an hour long run is shown in Figure 1.1. The detector sensitivities for all beam parameters for a few days during Run 1 are shown in Figure 1.2. Beam modulation amplitudes at the target, as well as typical monthly results measured for the HC

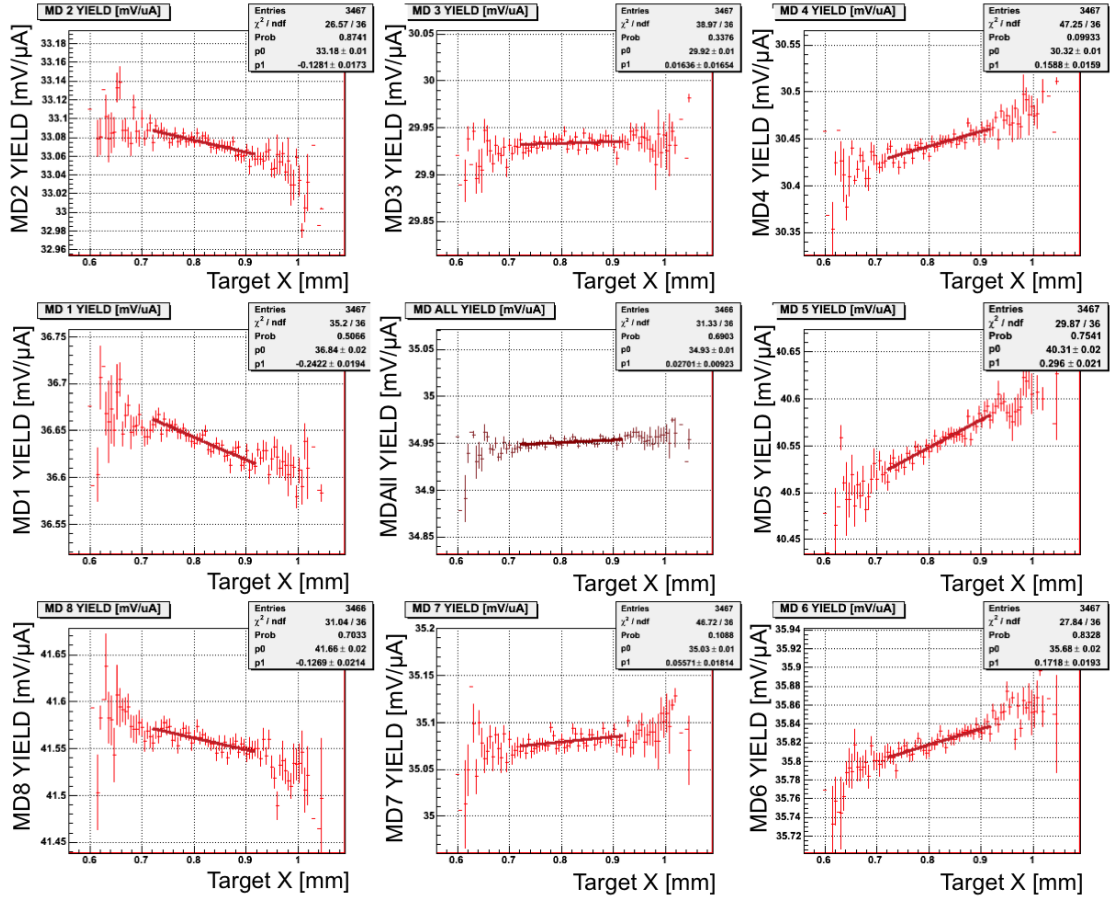


Figure 1.1 Main detector sensitivities with respect to target BPM X position for X Position Modulation.

beam properties ΔT_i and detector sensitivities $\partial A / \partial T_i$ during Run 2 can be found in Table 1.1. The HC beam asymmetries for X, X' are anti-correlated and largely cancel. The same is true for Y and Y'. The uncertainties associated with the monthly HC position (angle) differences ΔT_i are 0.07 nm (0.01 nrad) based on the quartet level BPM resolution (discussed in section 1.4), shown in Table 1.1.

A subset of the Run 2 parity violating electron-proton scattering production data showing the blinded asymmetry grouped by (monthly) Wien state is shown in Figure 1.3 [1]. Two different approaches to determine the sensitivities of the apparatus to HC beam properties were used to correct for the false asymmetry. The measured asymmetries without any correction (solid squares) are compared to the asymmetries after correction using the intrinsic random variations in beam properties (natural motion: triangles) and to the asymmetries using the beam modulation (beam

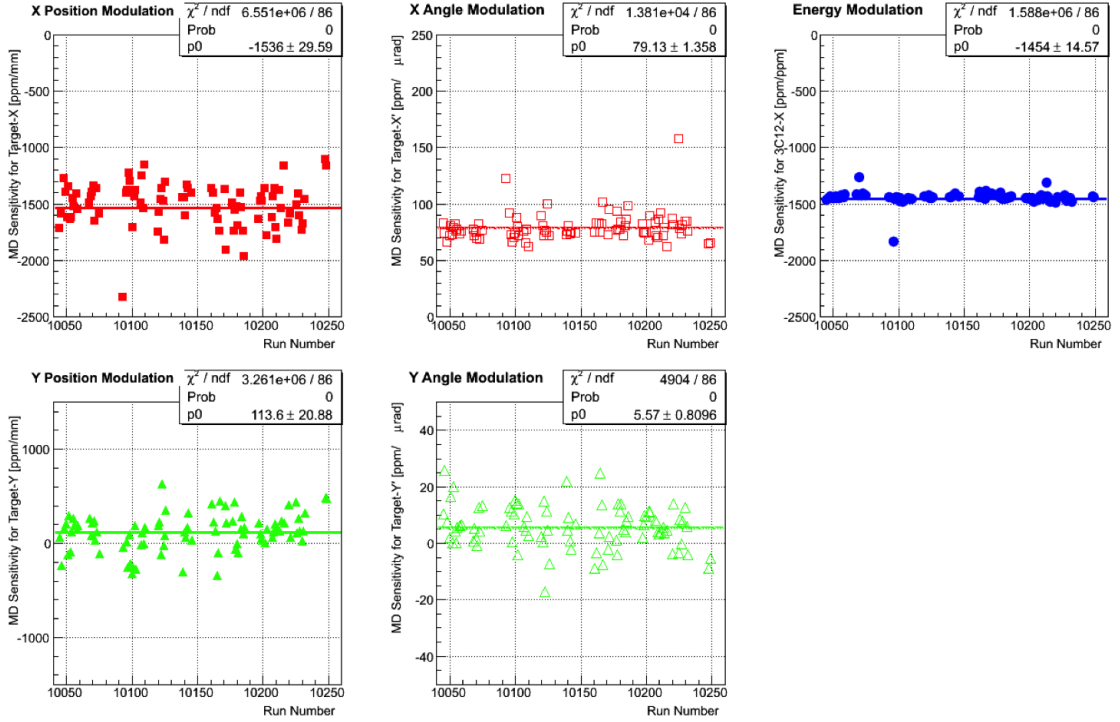


Figure 1.2 Main detector sensitivities for X (solid red square), X' (empty red square), E (solid blue square), Y (solid green triangle), and Y' (empty green triangle) are shown.

Table 1.1 A typical amplitudes used for driven beam modulation (column 2). Columns 3 and 4 provide typical average monthly results measured during Run 2 for the helicity correlated beam parameter differences ΔT_i and detector sensitivities $\partial A / \partial T_i$ for the beam parameters i listed in the first column. The total HCBA for this example is only 0.4 ppb. The uncertainties associated with ΔT_i and $\partial A / \partial T_i$ are discussed in the text [1].

Beam Parameter	Modulation Amplitude	Differences [monthly]	Sensitivities [monthly]
X	$\pm 125 \mu\text{m}$	-3.3 nm	-2.11 ppm/ μm
Y	$\pm 125 \mu\text{m}$	2.5 nm	0.24 ppm/ μm
X'	$\pm 5 \mu\text{rad}$	-0.7 nrad	100.2 ppm/ μrad
Y'	$\pm 5 \mu\text{rad}$	0.002 nrad	-0.0 ppm/ μrad
E	$\pm 61 \text{ ppm}$ (70 keV)	0.1 nm	-1.56 ppm/ μm

modulation: inverted triangles). The asymmetries derived using each techniques are consistent with each other, and the overall correction for HC beam asymmetries is small. The data shown here represent 80% of the Run 2 data for which modulation was available. An additional 1/3 of the total data acquired in the experiment was provided by Run 1 dataset. More detailed description of modulation sensitivity analysis and recent results will be discussed by J. Hoskins [2] and D. Jones [3] in their future theses.

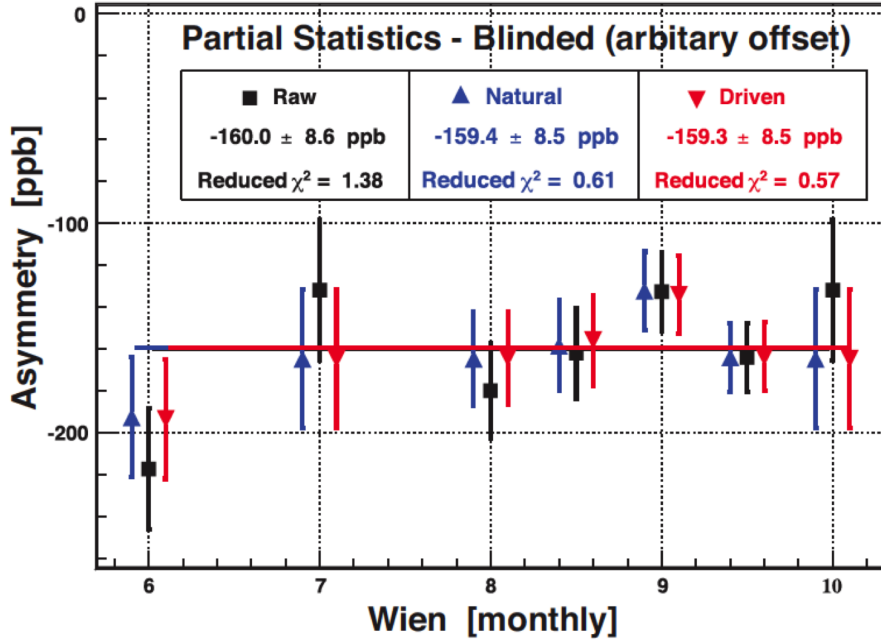


Figure 1.3 Subset of the Run 2 production data showing the blinded asymmetry (in ppb) grouped by (monthly) Wien state, and corrected using two different approaches to determine the sensitivities of the apparatus to HC beam properties that can give rise to false asymmetries. Other needed corrections are not applied to the data in this figure. The results without any correction (solid squares) are compared to the results after correction using the intrinsic random variations in beam properties (Natural motion: upward pointing triangles) and to the results using the driven beam motion (Beam modulation: downward pointing triangles) where the sensitivities are derived by actively modulating each property of the beam with a magnitude significantly larger than that intrinsically carried by the beam. The asymmetries derived using each technique are consistent with each other, and the overall correction for HCBAs is small. The data shown here represent the 80% of the Run 2 data for which driven motion was available. Run 1 provides an additional $\sim 1/3$ of the total data acquired in the experiment [1].

1.2 Beamlime Optics

A typical BPM response to modulation drive signal is sinusoidal and is shown in Figure ?? in the previous chapter. The responses from all 23¹ BPMs in the Hall-C beamline to modulation signal were observed throughout the production data collection. The BPM responses in X due to X modulation are shown in Figure 1.4. The vertical axis is the BPM X-signal for X kick and the horizontal axis is the phase (the ramp-wave was used to monitor the phase of the drive signals). The data are shown in red and fits are in dark red. The BPM responses are arranged according to the distance from the target. Beam position response amplitudes of all the BPMs to X modulation (from Figure 1.4)

¹There were 24 BPMs in the Hall-C beamline. BPM 3H09B died after Run 1, hence excluded from the analysis.

with respect to Z locations from the target are shown in Figure 1.5. The location of all the BPMs are shown at the top of the plot by short vertical lines. All the quadrupoles, dipoles, Compton dipoles, Møller magnets, target, and beam modulation magnets are shown by short vertical lines at the bottom. Data are shown in solid circles, and simulated points from OptiM are shown in empty squares. This figure represents the evolution of the position response amplitude to modulation drive signal along the Hall-C beamline. The data matches quite well with the simulation. This method of tracking BPM response also helped to find any optics change or hardware failure in the beamline.

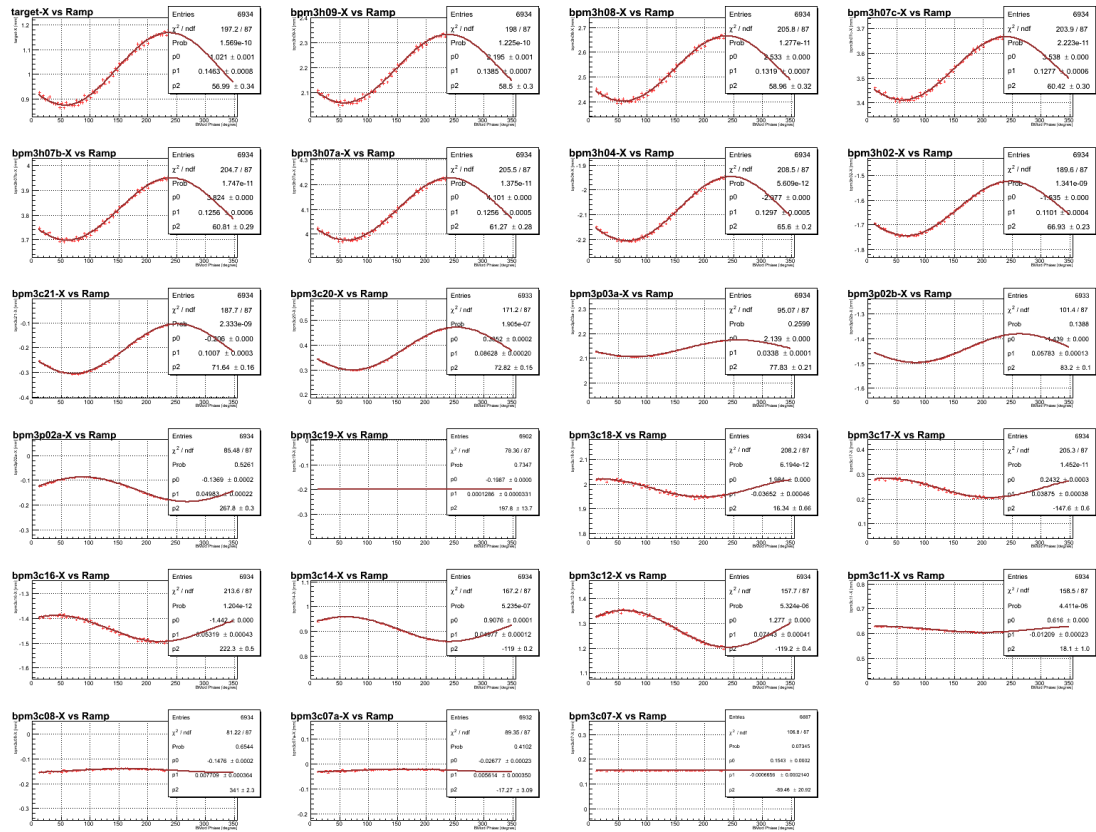


Figure 1.4 All Hall-C BPM responses in X due to X modulation using a pair of coils. The vertical axis is BPM X -response and horizontal axis is ramp-wave (the ramp-wave was used to monitor the phase of the drive signals). The data are shown in red and fits are shown in dark red. Starting at the target BPM in the top left, upstream BPMs are shown along the left to right and top to bottom directions, BPM 3C07 being the first BPM in the Hall-C beamline.

The BPM responses in X due to X' modulation, responses in Y due to Y modulation, responses in Y due to E modulation, and responses in X due to E modulation are shown in Figure 1.6 (from top left along the clockwise direction). The Fast Feed Back (FFB) system was fighting with the

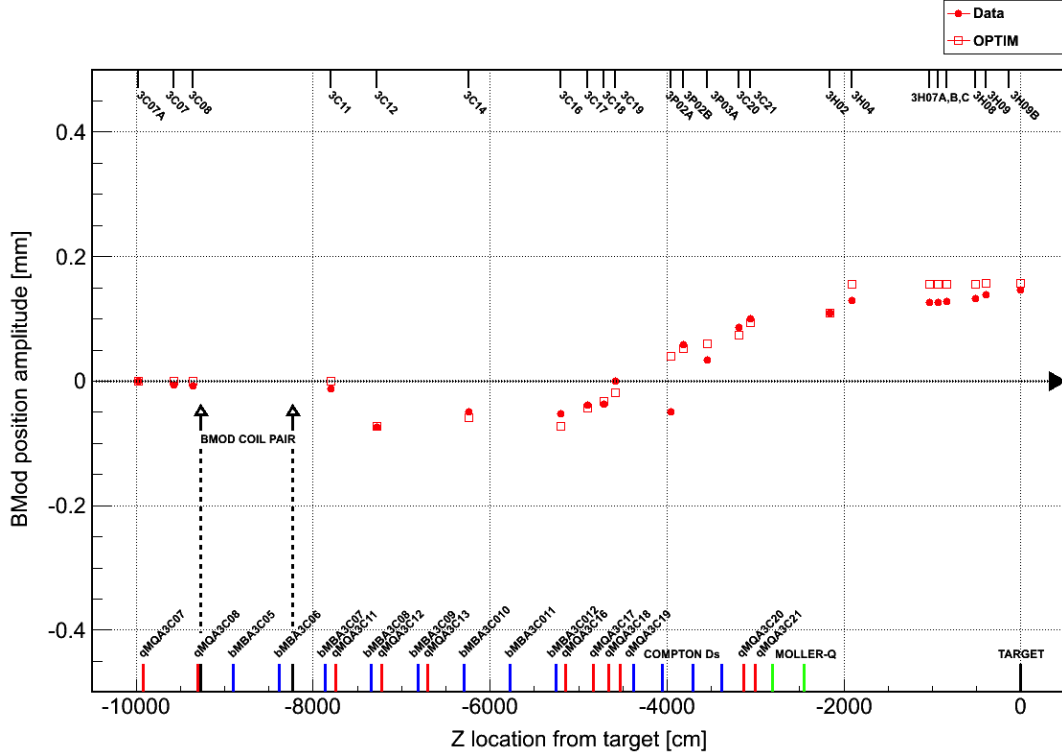


Figure 1.5 Beam position response of all the BPMs in the Hall-C beamline to X modulation. The locations of all the BPMs are shown at the top of the plot by vertical line. All the quadrupoles, dipoles, Compton dipoles, Møller magnets, target, and BMod magnets are shown at the bottom of the plot by vertical lines. Data are shown in solid circles, and simulated points from OptiM are shown in empty squares.

modulation system which is more evident in the X' modulation response (see section 1.2.3 for more details). There was a defocus in Y modulation and the system was not able to achieve a relatively pure Y position at the target. The residual dispersion at the target X was evident from the E modulation and was as high as $\sim 1/7$ th of the dispersion of the middle of the arc. The residual dispersion in Y was also non-negligible. These responses were recorded for all the production runs. The target BPM and BPM 3C12 position responses to X modulation vs. time for Run 1 and Run 2 are shown in Figure 1.7. The target X position was unstable at the beginning of the experiment. The big dip in the amplitude around run number 10900 was due to change in “tune” (BMod magnet current ratio) in order to achieve a better decoupling in the beam parameters. The optics was very stable from run number 11900 onward. There was a constant residual dispersion at the target throughout the experiment.

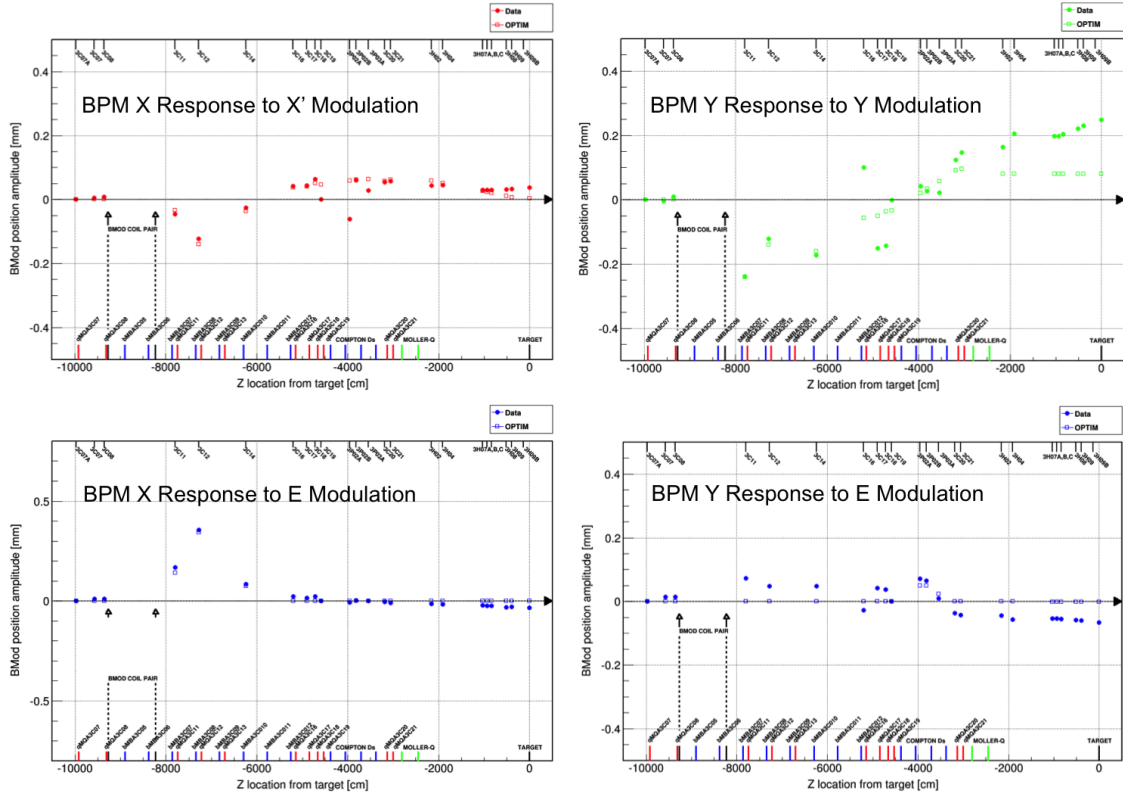


Figure 1.6 Beam position response of all the BPMs in the Hall-C beamline to X modulation. The locations of all the BPMs are shown at the top of the plot by vertical line. All the quadrupoles, dipoles, Compton dipoles, Møller magnets, target, and BMod magnets are shown at the bottom of the plot by vertical lines. Data are shown in solid circles, and simulated points from OptiM are shown in empty squares.

1.2.1 BPM Sign Corrections

The beam modulation system also helped to track some of the problems in the BPMs in the Hall-C beamline. During Run 1, BPM 3C19X (as shown in Figure 1.8) and Y showed no response to any modulation drive signals, whereas BPM 3C16Y showed an inverted response (more details in APPENDIX ??). After investigation, misconnected cables were found for those BPMs and repaired before Run 2. Another problem was found with the BPMs 3P02A and 3P02B in the Compton region. These Compton BPMs had a different rotation in the beamline compared to the all other BPMs, hence they responded differently to the modulation signal. This problem was fixed in the software by giving an offset angle for these BPMs. The BPMs discussed above did not affect any physics results for Run 1, as they were not used in any asymmetry or regression calculation.

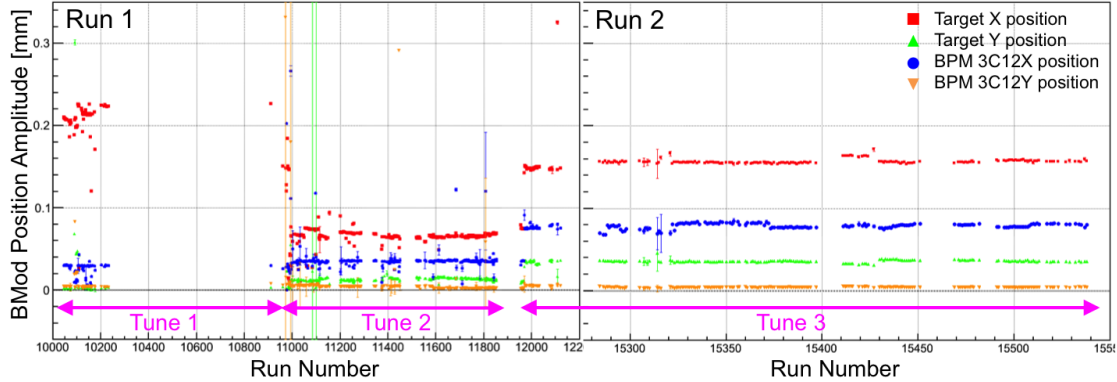


Figure 1.7 Hall-C target BPM responses due to modulation kick using a pair of coils in X. The sinusoidal response of the target BPM of a modulation signal for relatively pure X is fitted and the amplitude of the sinusoidal signal is plotted in vertical axis. The vertical axis is BMod BPM position in mm. The X target position is shown with solid red diamond, Y target position is shown with solid green triangle, BPM 3C12 X position is shown with solid blue square, BPM 3C12 Y position is shown with solid orange circle. For a relatively pure X position motion, we expect largely X target response and very small X angle response. We do not expect any Y position or Y angle response in this case. BPM 3C12X position response is relatively constant and 3C12Y is consistent with zero.

1.2.2 Beam Modulation Tune Parameter Scan

The idea of this analysis was to find a relatively pure angle and position “tune” at the target for the modulation system. In order to achieve a pure X and Y position and angle at the target, scan of the “tune” parameters was performed by varying the ratio of the drive signals in small steps. The maximum amplitudes of the function generator drive signals for this test were set to 0.444 times of the nominal amplitudes (shown in Table ??, chapter ??) for caution. The tune parameters were changed by changing the current in one coil (I_1) in steps of 50%, 25%, 0%, -25%, and -50% respectively keeping the other coil (I_2) fixed to achieve a “tune” that generates a relatively pure angle at the target. A relatively pure X-angle tune was found to be in between the tune parameters -5.882 (nominal) and -9.009 (53.2%), and Y-angle to be in between -0.500 (nominal) and -0.675 (35%). The “tunes” for X and Y positions were already good to produce relatively pure position at the target. Based on this analysis, the modulation “tunes” were changed during Run 1 and are shown in Figure 1.7.

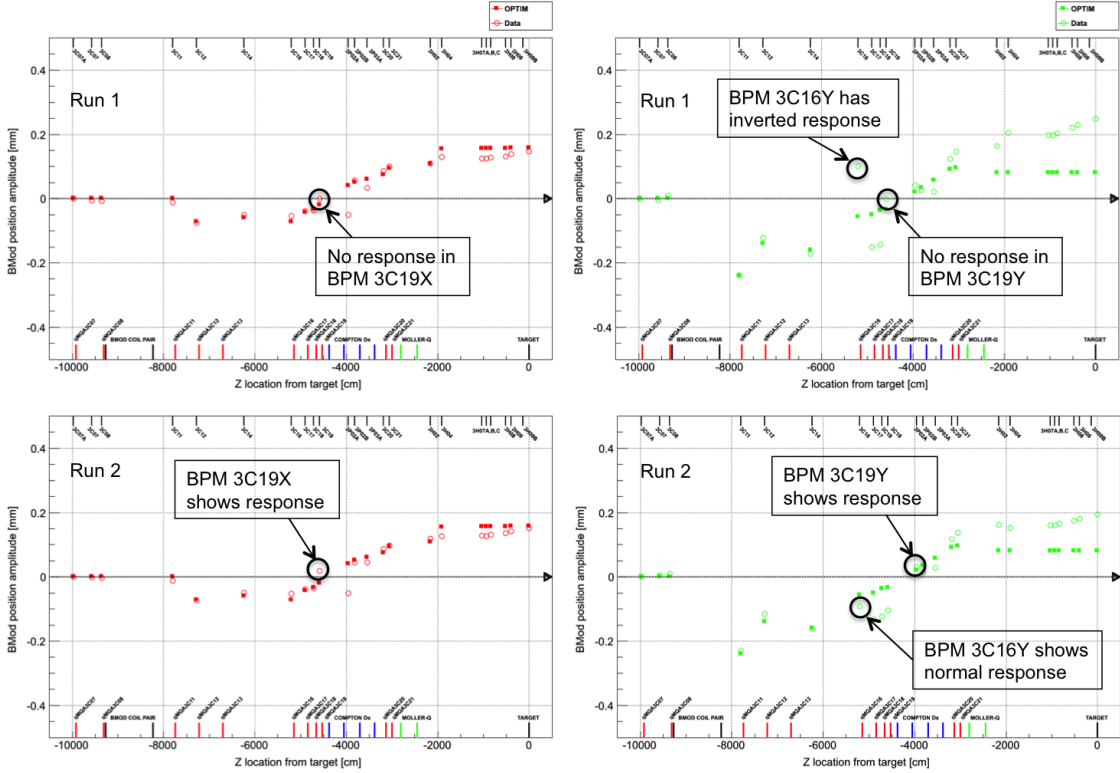


Figure 1.8 The beam position response of all the BPMs in the Hall-C beamline to X modulation. The locations of all the BPMs are shown at the top of the plot by vertical line. All the quadrupoles, dipoles, Compton dipoles, Møller magnets, target, and BMod magnets are shown at the bottom of the plot by vertical lines. Data are shown in solid circles, and simulated points from OptiM are shown in empty squares.

1.2.3 Effect of Fast Feed Back on Beam Modulation

The Fast Feed Back (FFB) system was designed to suppress any position and energy fluctuation in the beam position monitors. So it was important to inspect the effect of FFB system on the modulation system. The beam position responses of all the BPMs in the Hall-C beamline to X' modulation for FFB ON (by red empty circles) and OFF (by black empty triangles) are shown in Figure 1.9, respectively. The simulated position responses from OptiM are also shown in the figure (by solid red squares). The driven signals were 0.444 times of the nominal amplitudes for this test (shown in Table ??, chapter ??) for caution. There were minimal effects of FFB on BPM responses amplitude for X, Y and Y' modulation (see APPENDIX ??), but noticeable suppression was observed for X' modulation (see Figure 1.9). This preliminary study exhibited no big position suppression of the BPM responses amplitude due to FFB system, as shown in Figure 1.9, although the effect on the phase of the BPM response along the beamline was not insignificant [4]. The FFB was

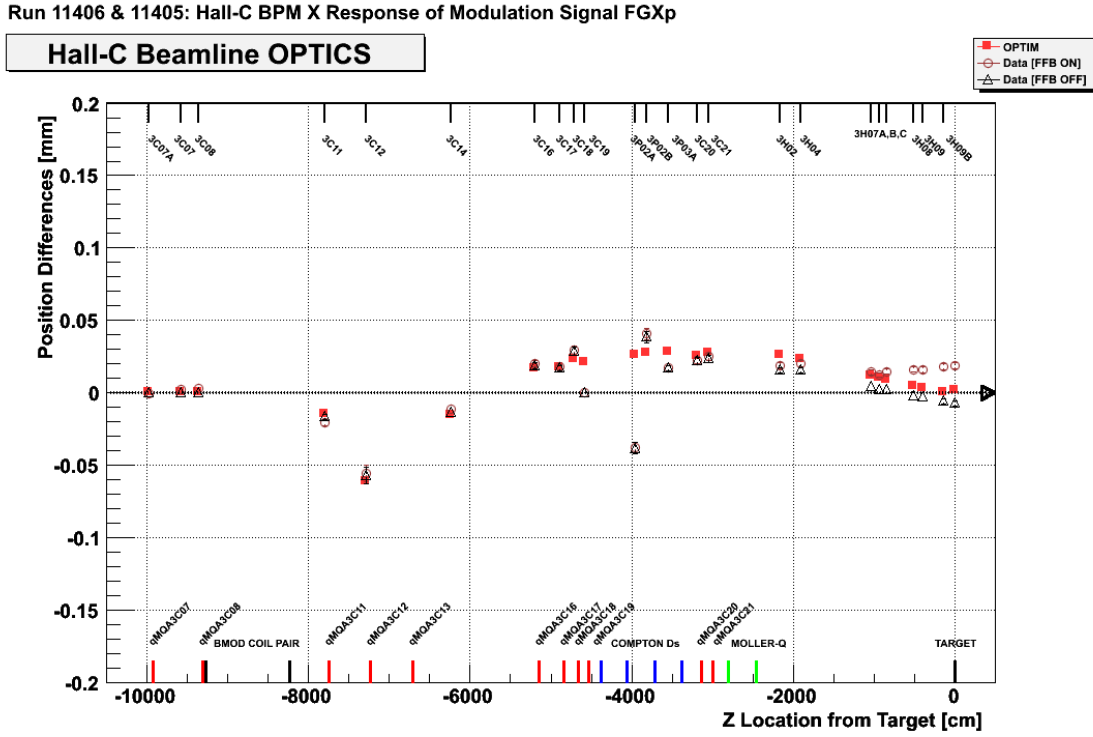


Figure 1.9 Hall-C BPM responses in X due to X angle modulation using a pair of coils. The vertical axis is BPM X-signal amplitude and horizontal axis is beamline elements. The simulated points from OptiM are shown in solid red squares, data with FFB ON are shown in empty red circles and data with FFB OFF are shown in empty black triangles. There is almost no effect of FFB on data for X motion. The locations of all the BPMs are shown at the top of the plot by vertical lines. All the quadrupoles, dipoles, Compton dipoles, Møller magnets, target, and BMod magnets are shown at the bottom of the plot by vertical lines.

not paused during position modulation and might have been responsible for the phase slip in BPM responses. Originally FFB was paused during Run 1 during position modulation, and the energy was also locked during energy modulation. In an effort to be less invasive during production running, the FFB was always kept on for position and angle modulations, and number of energy modulation cycles was reduced to half during Run 2. A new analysis approach was used to counter the phase slip problem [5]. The position-dependent phase slip was assumed to be a sum of modulation from two different locations, and two independent transfer functions from each of the driving locations can be used to decompose the response. The FFB response can be decomposed into a combination of two harmonic functions, one sine and one cosine, that match phases with the modulation drive signals. The FFB sine response combined with modulation drive sine function become the effective

driving signal and FFB cosine response averages to zero amplitude for the sine fit. More details on the analysis will be discussed by D. Jones [3] in his future thesis.

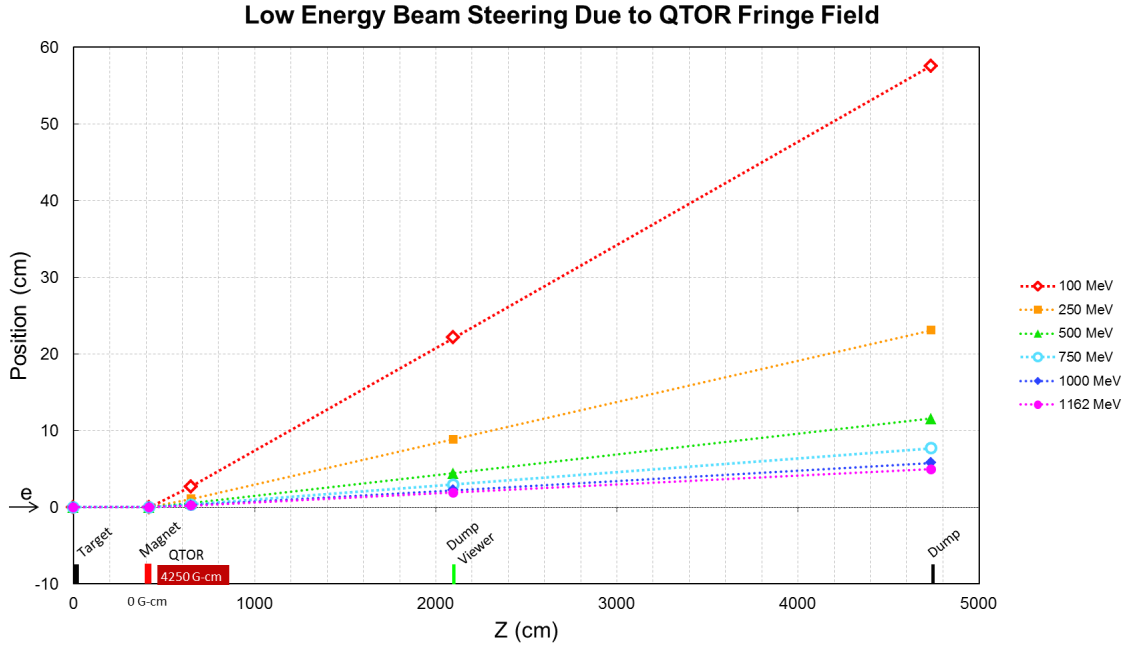


Figure 1.10 QTor all energy 0 G-cm.

1.3 QTOR Fringe Field and Optics Change

There was a vacuum leak activated by heating due to low energy electrons near the beam dump during Run 1. This unplanned event forced a delay in the experiment for months. Smaller bellows diameter with two stainless steel flanges might have been activated due to low energy electrons coming from upstream which might have caused the vacuum leak. It was found that the QTor has a non-zero field integral along the beam axis and might have deflected the low energy electrons in the dump viewer flanges. So, the plan of the collaboration was to improve the hardware assembly near the beam dump with a larger bellows diameter (see Figure 1.11 top panel) before Run 2. The new structure was built to minimize the stainless exposure, and low energy electrons coming from radiative tail stripe landed on aluminum, which helped to reduce the activation (see Figure 1.11 bottom panel). Another strategy was to design and build a corrector magnet to counter steer the fringe field of the QTor.

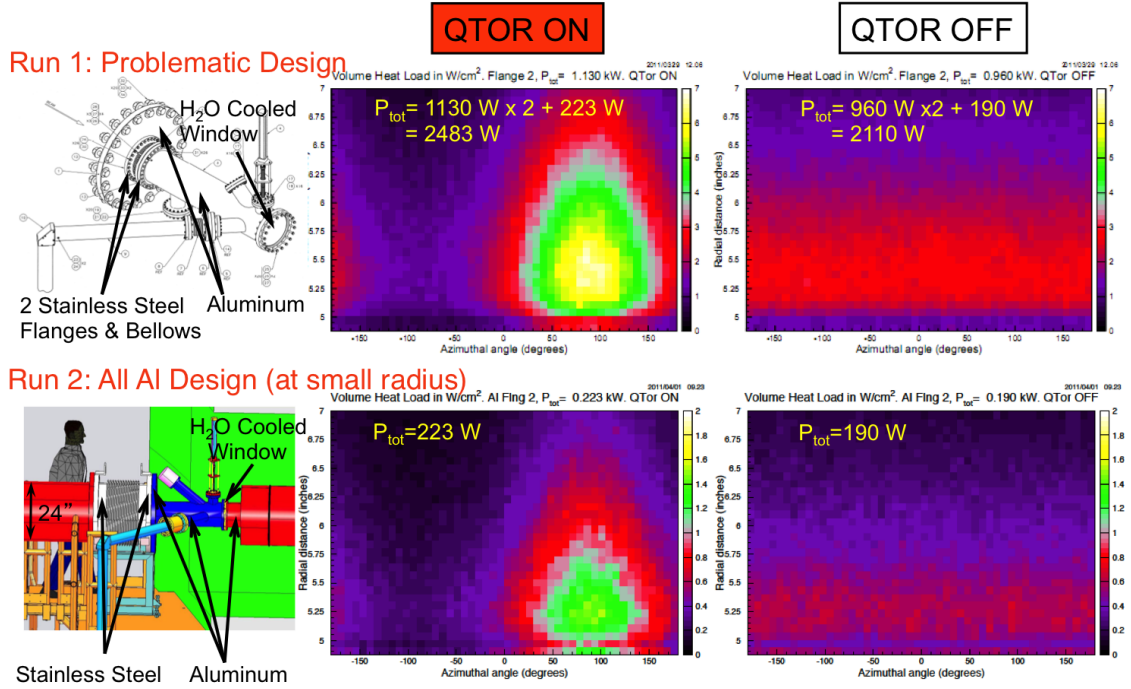


Figure 1.11 Bellows hardware and vacuum heat load before and after the activation. The top panel shows the Run 1 hardware of the bellows in the left and volume heat loads in the flange during QTor ON and OFF respectively. Run2 bellows hardware and volume heat loads are shown in the bottom panel.

At the beginning of the experiment, it was observed that QTor steers the forward beam and one important question was to examine whether the steering could be caused by the expected QTor fringe field along the beam axis, or whether the steering indicates misalignment or motion of any coils. The primary beam (1.2 GeV) spot moved ~ 2 cm on the dump viewer between QTor OFF and ON. The magnet steered the beam up and right towards the observed hot spot in the dump viewer (see Figure 1.11 top panel). The steering implies a residual field integral of 4250 Gauss-cm in QTor. The natural fringe field near the axis of an ideal eight-fold toroid scales like r^7 [6], and was not strong enough to cause the observed steering unless the beam was many centimeters away from the axis for most of the length of the toroid. However, a radial shift of one coil by 3 mm generates a large enough residual field on the axis to steer the beam as observed. The effect of the QTor fringe field (4250 Gauss-cm) along the beam axis was simulated using OptiM [7]. The simulation conditions were as follows:

- QTor and dump viewer in the OptiM model were added to the Q-weak main input deck [8] for this analysis.

- No microscopic model of the QTor field symmetry breaking was used. The QTor region was treated as a 4 m long dipole with a 4250 Gauss-cm field integral.
- Earth's magnetic field was ignored in the simulation.

A beam steering of ~ 2 cm at the beam dump viewer due to QTor fringe field (4250 Gauss-cm) was observed in the simulation for the primary electron beam (1.2 GeV) and confirmed the earlier observation. The effect of the fringe field on lower energy electrons was much higher, and the simulated tracks are shown in Figure 1.10 [9].

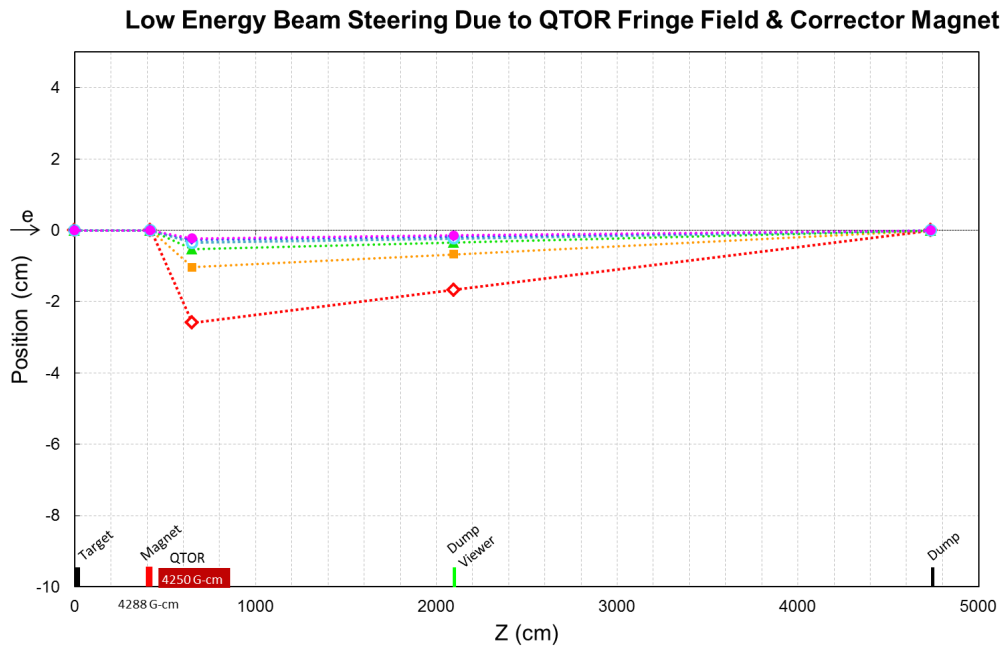


Figure 1.12 QTor all energy 4000Gcm dump.

1.3.1 QTOR Corrector Magnet

The next step was to design a corrector magnet that could suppress the fringe field in the QTor and fit into existing beamline structure. The ideal location for the corrector magnet was simulated to be in front of the QTor [10]. The estimated magnet field strength for the corrector magnet, placed before QTor, to compensate beam steering due to the QTor fringe field was ~ 4000 Gauss-cm. The effect of the corrector magnet on the QTor fringe field is shown in Figure 1.12. Besides containing the primary electrons, the corrector magnet also helped in suppressing the lower energy

electrons [11]. The corrector magnet had a bedstead structure and was designed using TOSCA [12,13] (see Figure 1.13).

Table 1.2 The design parameters for the QTor corrector magnet.

Parameters	Inner	Outer
X-radius [cm]	14.0	28.0
Y-radius [cm]	20.0	32.0
Z-length [cm]	8.0	10.0
Cross section [cm ²]	2.5×4.0	2.5×2.5
Current [A]	2600	-1000
No. of turns	240	150
Length per turn [cm]	132.48	240.96
Current per turn [A]	10.84	6.67
Resistance [Ω]	1.15	1.30
Total length [cm]	34947	39727
Mass [kg]	11.87	13.49
Power [W]	149.56	64.38
Voltage drop [V]	13.79	9.65
Temperature rise [K/s]	3.23×10^{-2}	1.22×10^{-2}

The design parameters for the QTor corrector magnet are summarized in Table 1.2. There were some constraints designing the corrector magnet as follows:

- Space available for corrector magnet was 25.4 cm along Z-direction.
- Lower edge of collimator opening was ~40 cm from center of beam pipe.
- The beam pipe diameter inside QTor was 27.4 cm.
- The corrector magnet had to be non-magnetic material to reduce EM interference.

The corrector magnet was designed to fit in the available space in front of the QTor and was capable of producing the desired field to counter steer the QTor fringe field. The power dissipation, voltage drop, temperature rise, and other important parameters associated to the coils were calculated and showed promising behavior (more details in [14]). The corrector magnet sensitivity to position and angle changes in space was simulated using TOSCA by moving each coil individually in all possible orientations. The simulation yields the magnet to be mostly insensitive to the position and angle changes (more details in [15]).

The field integral produced by the corrector magnet is shown in Figure 1.14. The Figure 1.14 also shows the field along X and Y direction at the collimator opening. The variation of magnetic field along the different octants has also been studied [16] (see Figure ??, APPENDIX ??). The field seems to decay very fast along the radial direction. The summary of the magnet design can be

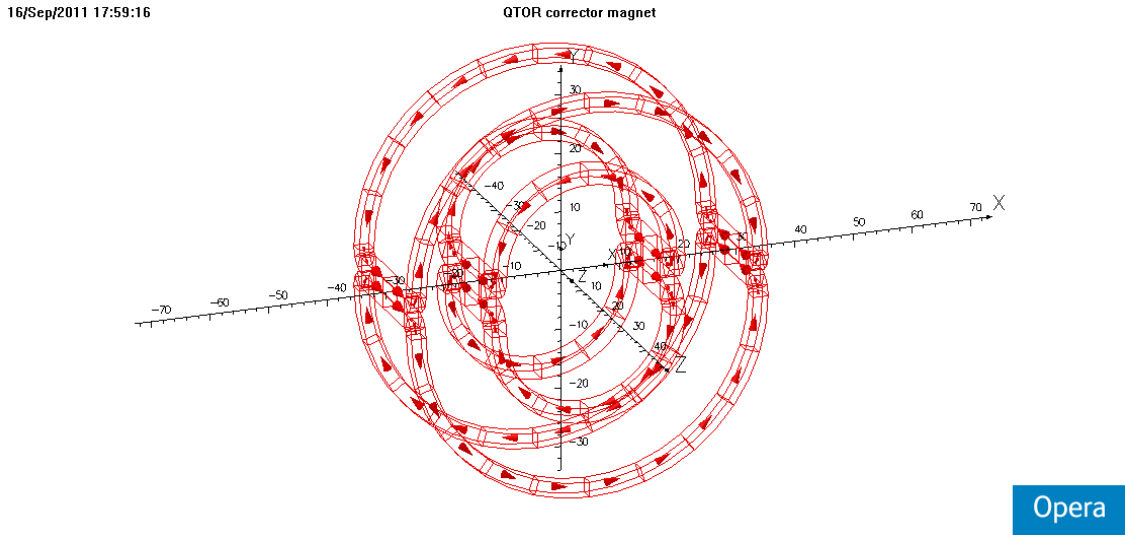


Figure 1.13 QTOR corrector magnet design.

found in [17]. As the hardware in the beam dump region was improved, it was decided not to build the corrector magnet in order to adhere to the schedule.

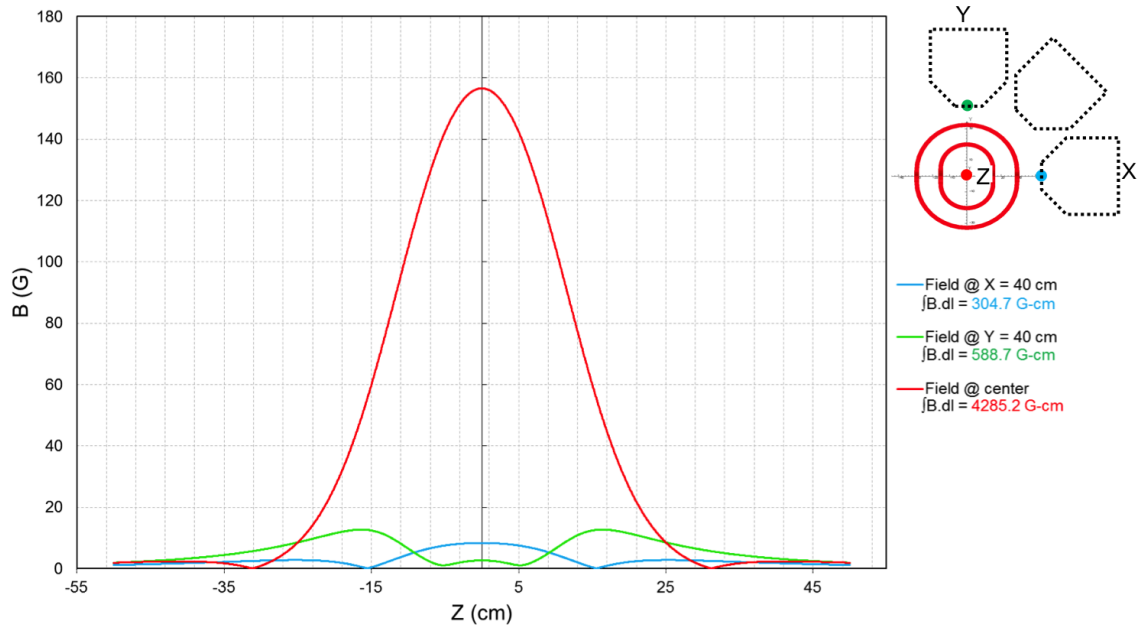


Figure 1.14 QTOR corrector field integral.

1.4 BPM Resolution

The BPMs in front of the target e.g; 3H09B, 3H09, 3H07C, 3H07B, and 3H07A were used for the linear regression as well as for the calculation of the virtual target BPM. Hence, it was important to know their position and angle resolutions. The BPM position resolution was extracted from the collected production data and the angle resolution was simulated using the relation between the position and the angle resolution at a fixed beam current.

1.4.1 Position Resolution

The target BPM is a virtual BPM calculated using five BPMs in the drift region (more details on virtual target BPM in section ?? and [18]). The position resolution of the BPM in front of the target was extracted by observing the residual of beam position differences (between two helicity states) on any BPM and the orbit projected from the target. This is expressed in Equation 1.4.1 (see cartoon diagram in Figure 1.16).

$$\begin{aligned} \text{BPM resolution} &\approx \sigma_{\text{Residual}} = \text{diff}_{\text{BPM}} - \text{Orbit Position Differences} \\ \text{Orbit Position Differences} &= (Z_{\text{BPM}} - Z_{Tgt})\text{diff}_{TgtSlope} + \text{diff}_{Tgt} \end{aligned} \quad (1.4.1)$$

Here diff_{BPM} represents the beam position differences between two helicity states, diff_{Tgt} represents the target position differences, $\text{diff}_{TgtSlope}$ represents the target slope differences, Z_{BPM} is the location of the BPM in the beamline, and Z_{Tgt} is the location of the target.

The average BPM resolution using selective data samples from the commissioning phase of the experiment (Wien 0) is found to be 0.70 and 0.77 μm for X and Y respectively at a fixed beam current of 145 μA . The position resolutions for all the BPMs in front of the target were stable during Wien 0 at fixed current and are summarized in Table 1.3. Y resolutions were quite similar to the X resolutions. An independent study of BPM 3H07B resolution by B. Waidyawansa [19] has shown that the resolutions of 0.945 ± 0.003 , and 1.060 ± 0.003 for X and Y respectively at beam current 150 μA and roughly agrees with this result. The BPM 3H09B had relatively good resolution but was not available during Run 2. The resolution for BPM 3H04 was poor, as shown in Figure 1.15 (b). This inconsistency might be due to the noise injected by the existing corrector magnets between the BPM 3H04 and 3H07A. The BPM 3H08 had a different hardware compared to the other BPMs. Hence, the BPM 3H04 and 3H08 were not included for the construction of the

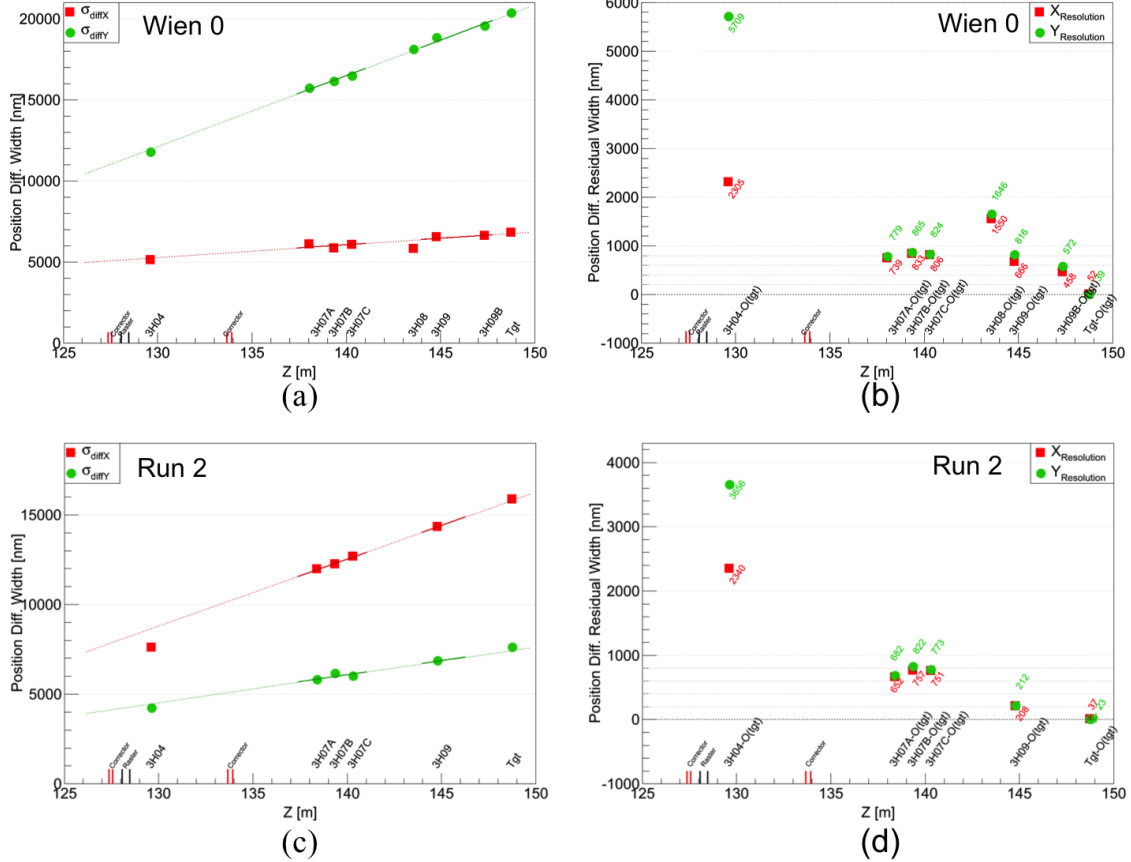


Figure 1.15 BPM position resolution. (a) Beam position differences for a typical one hour production run during Wien 0 at beam current of $145 \mu\text{A}$. Error weighted pol1 fits are shown by solid lines. BPM 3H04, 08 and, Tgt are not included in the fit. Fit is extrapolated using dashed line to guide the view. (b) Extracted BPM resolutions using (a) are shown for Wien 0 at beam current of $145 \mu\text{A}$. (c) and (d) show beam position differences and BPM resolution respectively for Run 2 at beam current of $180 \mu\text{A}$.

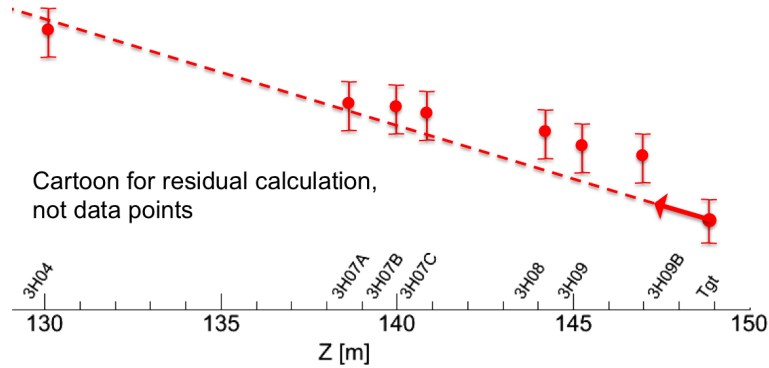


Figure 1.16 BPM resolution cartoon.

virtual target BPM. The same analysis was repeated for Run 2 with a beam current of $180 \mu\text{A}$, as shown in Figure 1.15 (c) and (d). The BPM resolution improves with the increase in beam current. A study of the BPM resolution variation with beam current can be found in [19].

Table 1.3 BPM position resolution at beam current of $145 \mu\text{A}$.

BPM	X Resolution [μm]	Y Resolution [μm]
3H09B	0.46	0.57
3H09	0.67	0.81
3H07C	0.81	0.83
3H07B	0.83	0.87
3H07A	0.74	0.78
3H04	1.70	3.55
Average (3H04 excluded)	0.70	0.77

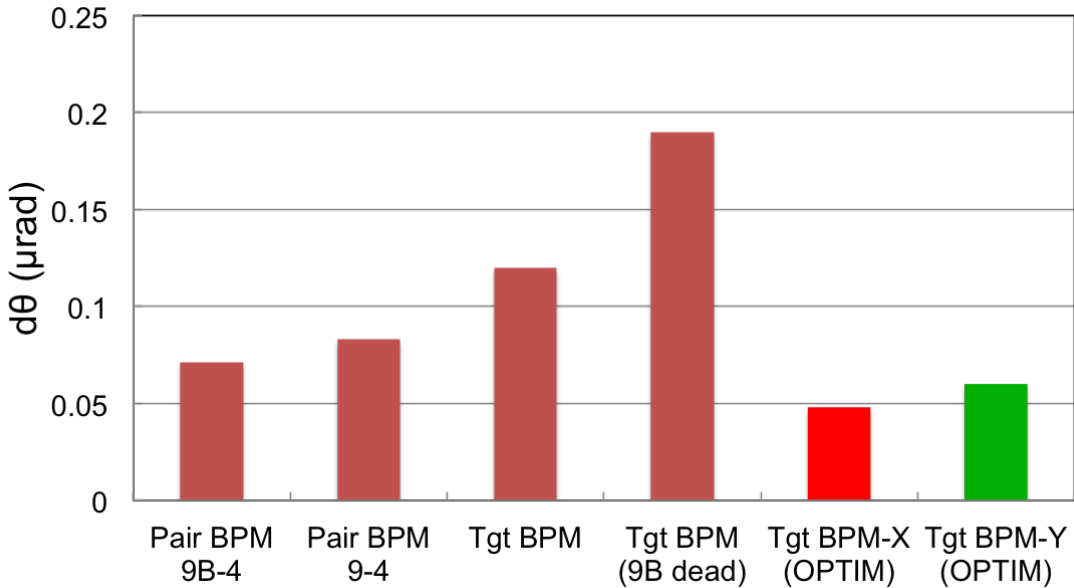


Figure 1.17 Target BPM angle resolution at beam current of $180 \mu\text{A}$.

1.4.2 Target BPM Angle Resolution

The target BPM angle resolution was simulated using OptiM [20]. In order to estimate the target BPM angle resolution, a relatively pure position measurement which corresponds to a pure angle measurement at the target was needed. A study of the strength sharing between angle and position in the various BPMs along the beamline for Wien 0 shows that the Compton BPMs (3P02A and B) were insensitive to the position at the target [21]. Then the known BPM position resolution and the

transport matrices between the Compton BPMs and the target BPMs were used to estimate effective angle resolution. Assuming the X(Y) position resolution to be 0.90 (0.96) μm , the estimated target BPM X (Y) angle resolution at a fixed beam current of 180 μA is 0.048 (0.060) μrad . A simple model calculation, where the angle jitter at the target corresponds to a pure position at BPM 3P02A (without using the transport matrix), agrees with this simulation. The simulated target BPM resolution in this analysis is better than the existing calculation with other BPMs [22]. A comparison of the resolution using different BPM pairs is shown in Figure 1.17.

1.4.3 Consistency Check of the Target Variable

The most commonly used independent variables for the linear regression were target positions and angles. So it was important to check the consistency of the target variable since it was created using 5 BPMs in the drift region in the beamline over a span of 10 m upstream of the target (more details about target variable can be found in section ?? and in [18, 23]). In order to check the consistency of the variable, the BPM differences used for the calculation were projected back to the target. A schematic diagram is shown in Figure 1.16. The beam position differences and the BPM residuals from the projected orbit are shown in the Figure 1.18. The target BPM was consistent, but the target intercept in the Q-weak database sometimes was significantly inconsistent and made χ^2/DOF of the fit worse. As in the regression or any of the Q-weak calculations, the intercept was not used, hence this inconsistency in the intercept did not make any impact on the physics result. A linear fit of the BPMs in front goes through the target BPM within 0.03 nm. The X position differences uncertainties are usually underestimated; this is necessary to assign the uncertainties in the regression. The BPM 3H04 effectively has the wrong units in the analysis software and a scale factor of 0.75 can eliminate this inconsistency. It is not very clear yet how big a problem this is for regression, since 3H04 was used in few regression schemes. The beam jitter was stable and Y jitter was larger than X jitter during Wien 0, but X jitter became larger than Y during Run 2.

1.5 Helicity Correlated Pedestal Analysis

The Q-weak collaboration proposed to measure the small parity violating asymmetry (~ 250 ppb) in elastic electron-proton scattering precisely [24]. The goal of the collaboration is to reduce any false asymmetry from various sources. One such potential source is helicity correlated pedestal differences for different detectors. The beam off detector yields at nominal operation and settings are known as

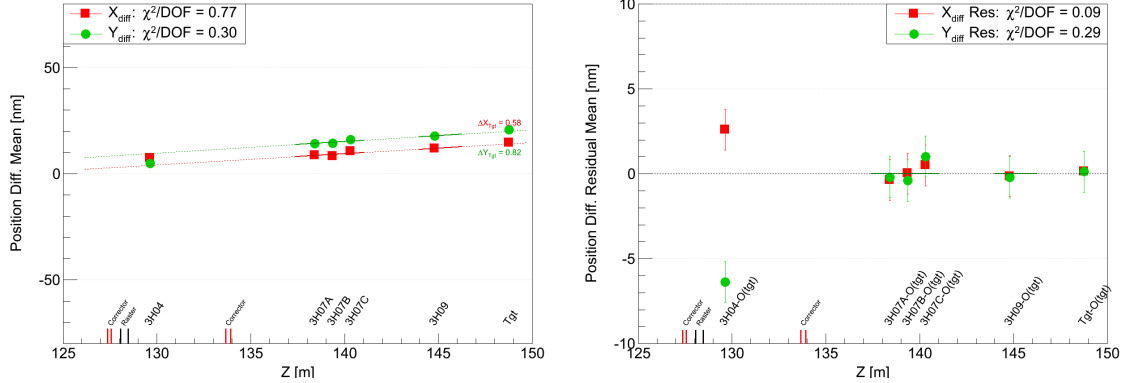


Figure 1.18 Target BPM consistency check. Beam position differences for a typical one hour production run during Run 2 at beam current of 180 μA are shown in (a). Error weighted pol1 fits are shown by solid lines. BPM 3H04, 3H08 and, Tgt are not in the fit. Fit is extrapolated using dashed line to guide the view. The residual of the BPM position differences and extrapolated orbit from target are shown in (b).

pedestals of that detector. Pedestal can be determined by the preamplifier offset and backgrounds with beam off data.

1.5.1 Motivation

A helicity correlated pedestal difference is a detector pedestal that is consistently different between the two helicity states. Any non-zero helicity correlated pedestal differences can cause false asymmetries in the measured parity violating asymmetry. The stability of the detector pedestal in the current mode (Y_{ped}) is directly related to the detector yield determination and can affect the detector linearity and asymmetry calculation. Helicity correlated pedestal differences could occur in many possible ways. One such process can be leakage from the pockel cell's high voltage which can change the polarization of the laser light that produces electrons from the photocathode. Main detectors, luminosity monitors and beam charge monitors need to be isolated from this pockel cell voltage flip in order to suppress helicity correlated pedestals. A small mV level leakage can create a huge false asymmetry (as shown in Equation 1.5.2), making this the primary motivation to monitor helicity correlated pedestal differences throughout the experiment.

1.5.2 Analysis Procedure and Goal

Typically, 5 minutes of dedicated beam off pedestal runs were taken during production running once a day during Run 1 and once every eight hours during Run 2. There were also ~ 1 hour

long beam off pedestal runs taken throughout, whenever there was an opportunity (for details see section ??, APPENDIX ??). The purpose of these pedestal runs was to minimize nonlinear distortions of asymmetries due to incorrect pedestals in the main detectors in the DC regime and estimate false asymmetry due to leakage current [25, 26]. The goal of this analysis is to survey the helicity correlated pedestal differences and raw pedestal signal for the entire experiment. The mean of the helicity correlated pedestal differences distribution gives an idea about the scale of false asymmetries and its width conveys a sense about the electronic chain noise level. Studying raw pedestal signals also helps to estimate the detector non-linearity due to wrong pedestals and the rms width of the raw signal provides an impression about the detector resolution.

1.5.3 Experimental Method

For a quartet of "+ - - +", measured asymmetry can be expressed as

$$A_M(+--+) = \frac{S_1^+ - S_2^- - S_3^- + S_4^+}{(S_1^+ - P) + (S_2^- - P) + (S_3^- - P) + (S_4^+ - P)}, \quad (1.5.1)$$

where S 's are the detector signals and P is the detector pedestal. A typical beam ON detector signal size was ~ 6 V. In order to estimate false asymmetry due to helicity correlated differences, consider a $0.01 \mu\text{V}$ voltage difference between + and - helicity states for the nominal detector signal. Then a false asymmetry due to this voltage difference can be calculated as

$$\frac{0.01 \times 10^{-6} \text{ V}}{6 \text{ V}} = 1.7 \times 10^{-9} = 1.7 \text{ ppb}. \quad (1.5.2)$$

The magnitude of the expected measured asymmetry for the Q-weak experiment is ~ 250 ppb. From the example in Equation 1.5.2, the false asymmetry can be 0.7%. To sense the effect of a wrong raw pedestal signal, consider a typical 120 mV pedestal error in a 6 V signal as an example. Then the potential non-linearity due to this error in the detector can be written as

$$\frac{120 \times 10^{-3} \text{ V}}{6 \text{ V}} = 2\%. \quad (1.5.3)$$

As shown in the above examples, a small leakage in the pockel cell's high voltage and wrong pedestal measurement can create significant false asymmetries in the measured asymmetry and non-linearity in the detector signals. So it was important to survey helicity correlated pedestal difference for the important detectors that can impact the Q-weak measured asymmetry.

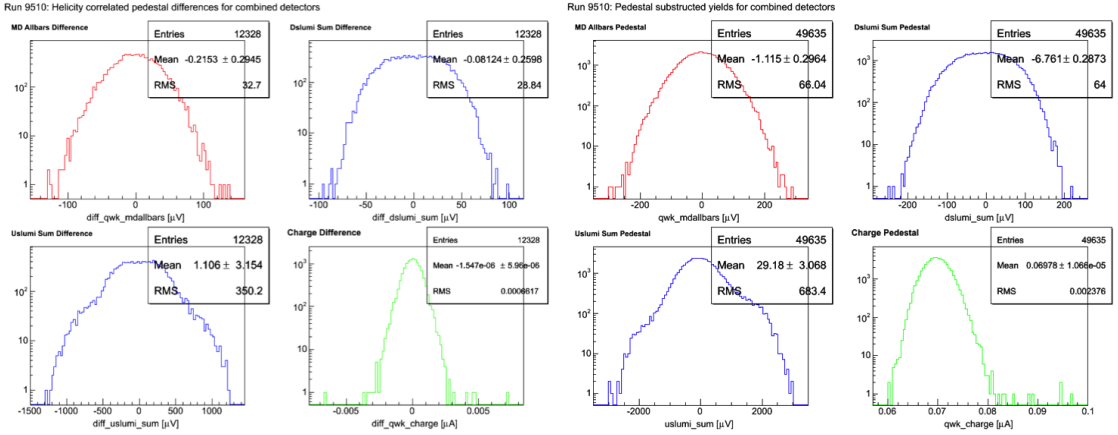


Figure 1.19 A typical beam off pedestal run (run# 9510). Helicity correlated differences for MDAllbars, DSLumiSum, USLumiSum, Charge (clockwise from top left corner) from Hel_Tree are shown in the left panel. Pedestal subtracted signal for MDAllbars, DSLumiSum, USLumiSum, Charge (clockwise from top left corner) from Mps_Tree are shown in the right panel.

1.5.4 Results

The main detectors and luminosity monitors are normalized to the charge monitors so it is important that neither have any evidence of helicity correlated pedestal differences. Helicity correlated differences from Hel_Tree of a typical 5 minutes pedestal run are shown in Figure 1.19. Even with only 5 minutes of data, no evidence of any helicity correlated pick ups for combined Čerenkov main detector (MDAllbars), downstream luminosity monitor (DSLumiSum), upstream luminosity monitor (USLumiSum), and beam charge monitor (Charge) were seen. The channels surveyed during this analysis are 17 MDs, 9 DSLumis, 9 USLumis, and 9 BCMs (details of the variables are described in APPENDIX ??, section ??). The individual channels of the MDs, DSLumis, USLumis, and BCMs showed no significant pickup. All these channels were investigated individually for each run and then averaged (error weighted) over a Wien². The Wien averaged helicity correlated differences for most important channels for the experiment MDAllbars, DSLumiSum, USLumiSum, and Charge³ are shown in Figure 1.20.

²Experiment has total 11 Wien period. Double Wien filters were rotated to change the electron beam polarization. This help reducing the false asymmetry.

³Charge = bcm1 + bcm2 for Run 1 and = bcm8 for Run 2.

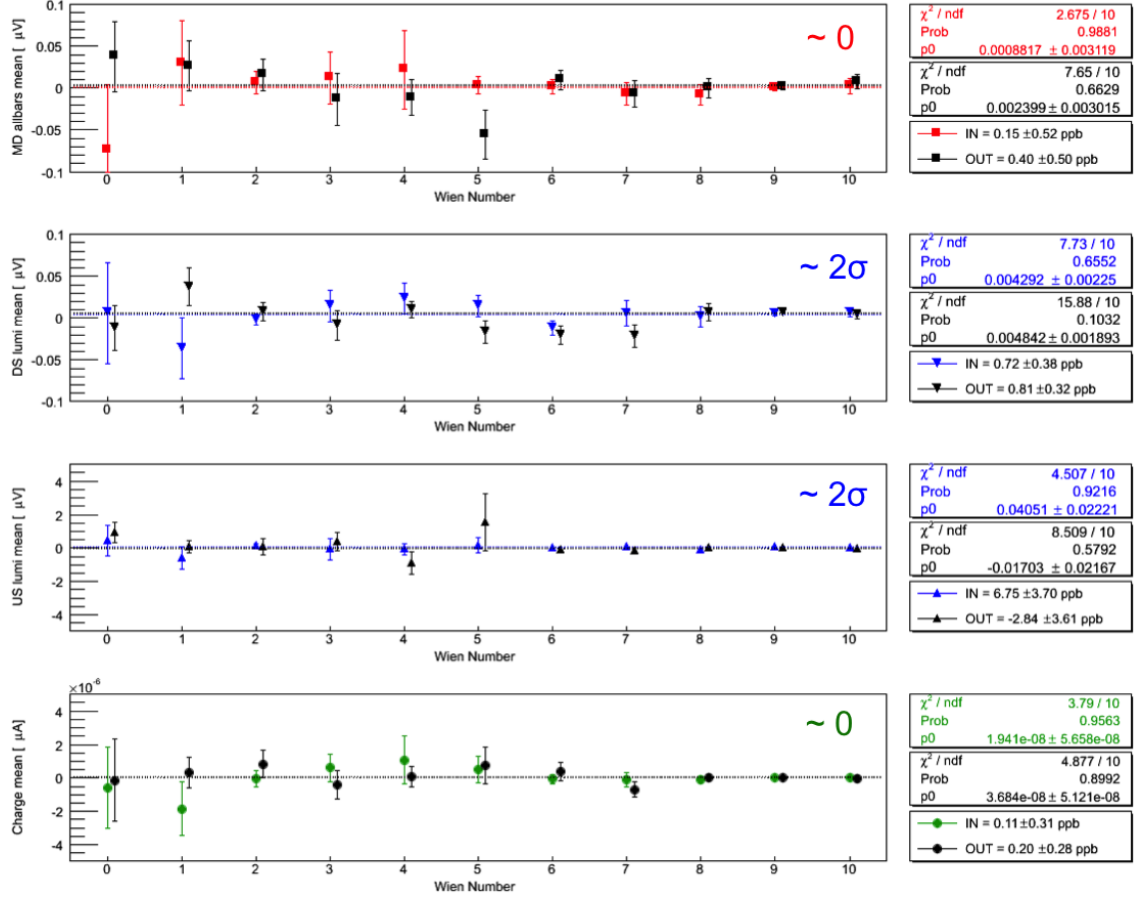


Figure 1.20 The mean of the pedestal differences from Hel_Tree for MD allbars, DS lumi, US lumi and Charge are shown. Each data point is averaged over a Wien. Two half wave plate states are shown separately.

1.5.4.1 Helicity Correlated Pedestal Signal Pickup

The mean of the pedestal differences from Hel_Tree in Figure 1.19 represent the helicity correlated pickup by a device. The surveyed result shows that the average pickup for MD is 0.15 ± 0.52 ppb for insertable half wave plate (IHWP) IN, and 0.40 ± 0.50 ppb for IHWP OUT (shown in Figure 1.20 by colored and black data points respectively). So helicity correlated pedestal differences have negligible contribution ($\sim 0.2\%$) to any false asymmetries in the measured asymmetry. DS Lumi has a similar level of pickup as the MD. US Lumi shows ~ 7 ppb pickup in worst case scenario which can be improved by using a better pedestal subtraction. BCMs have no pickups for the whole experiment. Overall pickup was much smaller during Run 2 (Wien 6 - 10) compared to Run 1 (Wien 0 - 5), and Run-0 (Wien 0).

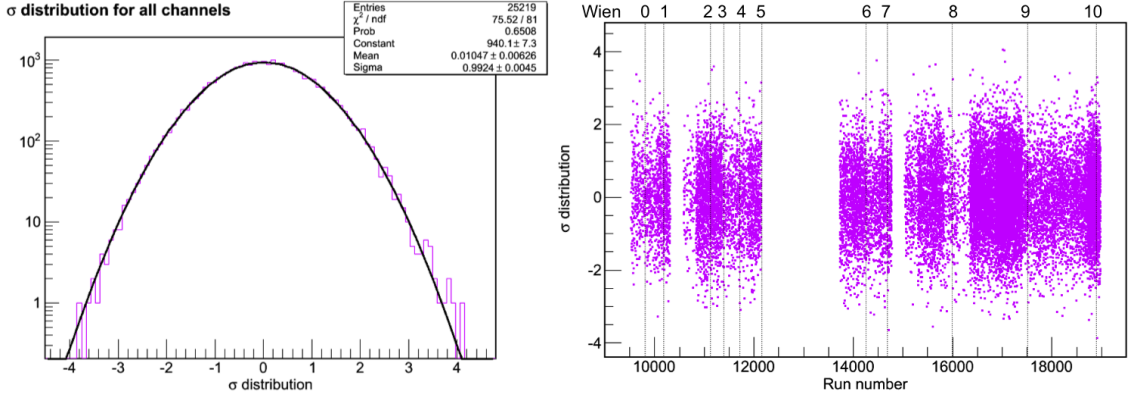


Figure 1.21 The pull distribution of helicity correlated pedestal differences for all channels and Wien (left). The pull of helicity correlated pedestal differences vs run number for all the channels are shown (right).

A pull variable helps to evaluate data points that pull the mean of the distribution and can be defined as

$$\sigma(ped)_{i,j,k} = \frac{\langle P \rangle_{i,j,k}}{error_{i,j,k}} \quad (1.5.4)$$

where $\langle P \rangle$ is the mean helicity correlated pedestal difference and the indices i,j,k denote channel number, run number and IHWP state respectively. The distribution of $\sigma(ped)_{i,j,k}$ for each channel and run is shown in Figure 1.21. The distribution of $\sigma(ped)_{i,j,k}$ is Gaussian and the mean is zero for each channel and run. The few σ from zero pickup for different detectors are within the statistical fluctuation. Mean of the helicity correlated differences for important background detectors (MD9, PMT only, PMT lightguide) were zero within $\sim 1\sigma$ for each Wien whereas for other background detectors pickups were zero within $\sim 3\sigma$. Several channels were examined in many pedestal runs, hence it was not unexpected to find a few channels that were non-zero by $3-4\sigma$ off the mean.

1.5.4.2 Helicity Correlated Pedestal Sensitivities

The helicity correlated pedestal difference width from Hel_Tree represents the sensitivity of a device to the helicity. It also depicts the measure of the electronic noise level for the detectors with low frequency rejection. The Wien averaged helicity correlated differences width for MDAllbars, DSLumiSum, USLumiSum, and Charge are shown in Figure 1.22. The average noise level of MDAllbars was $25 \mu V$. The MDs and the DSLumis noise levels were acceptable and well behaved throughout the experiment. USLumi electronic noise could have limited the detector's resolution

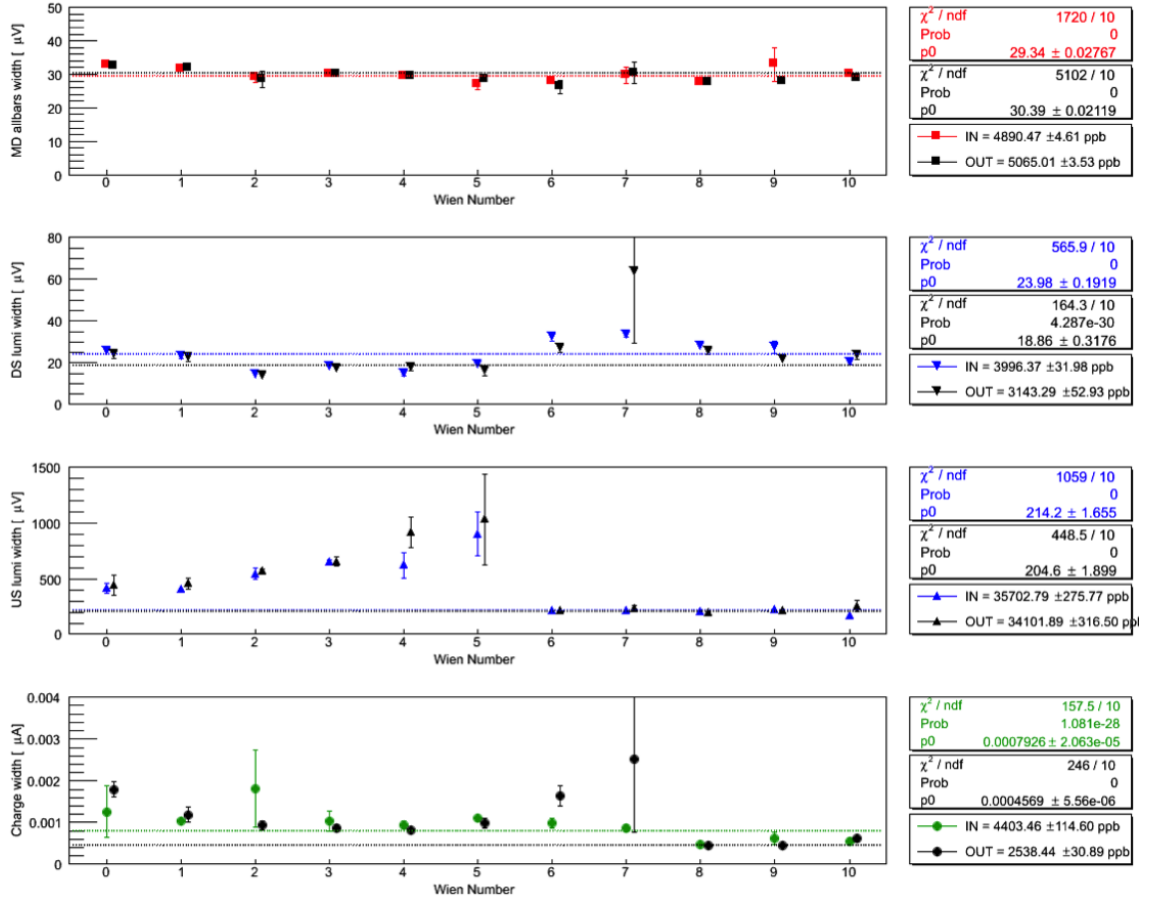


Figure 1.22 The width of the pedestal differences from Hel_Tree for MDAllbars, DSLumiSum, USLumiSum and Charge are shown.

near the end of Run 1, but improved in Run 2 after hardware repairs. Background detectors noise levels were reasonably stable during the experiment.

1.5.4.3 Stability of Pedestal Subtracted Signal

The mean of pedestal subtracted signal from Mps_Tree represent the relative change in pedestal signal compared to last pedestal. A wrong pedestal for a detector can cause nonlinearity in the detector system. MD pedestal was good to less than a mV (Figure 1.23). This results a nonlinearity of $\ll 0.1\%$ for 6 V signals. The detector yields are smaller for Aluminum and N \rightarrow Δ running compared to normal production running. The signal sizes are $\sim 30\text{-}40\%$ of 6 V. So the nonlinearity for these cases are higher but still $< 1\%$, allowing for smaller yields. DSLumi pedestal was off by at most 34 mV. The resulting nonlinearity would be $< 1\%$ assuming 6 V signals. To support Aluminum

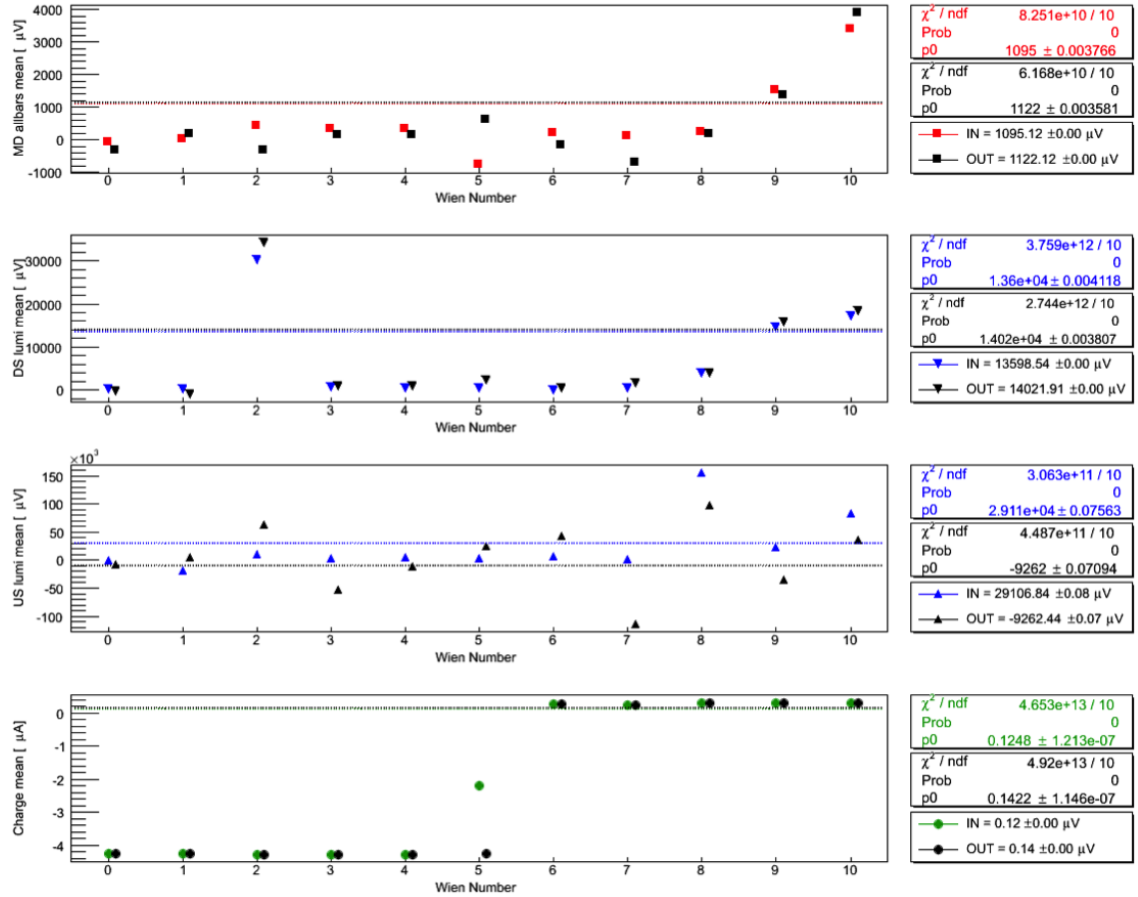


Figure 1.23 The mean of pedestal subtracted signal from Mps_Tree for MDAllbars, DSLumiSum, USLumiSum and Charge are shown.

and $N \rightarrow \Delta$ running, pedestal subtraction should be improved in Wiens 2, 9, 10. USLumi pedestal was off by 100-150 mV in Wiens 7, 8 and could result a nonlinearity of several percent.

1.5.4.4 Detector Resolution

The width of pedestal subtracted signal from Mps_Tree describes the measure of detector resolution. Resolutions for MDs and DSLumis were very good ($\sim 70 \mu\text{V}$) and reasonably stable during the experiment (see Figure 1.24). USLumis resolutions were ~ 15 times worse than MDs and DSLumis but were very stable. The resolutions for charge monitors and background detectors (except PMT LED) were steady throughout the experiment.

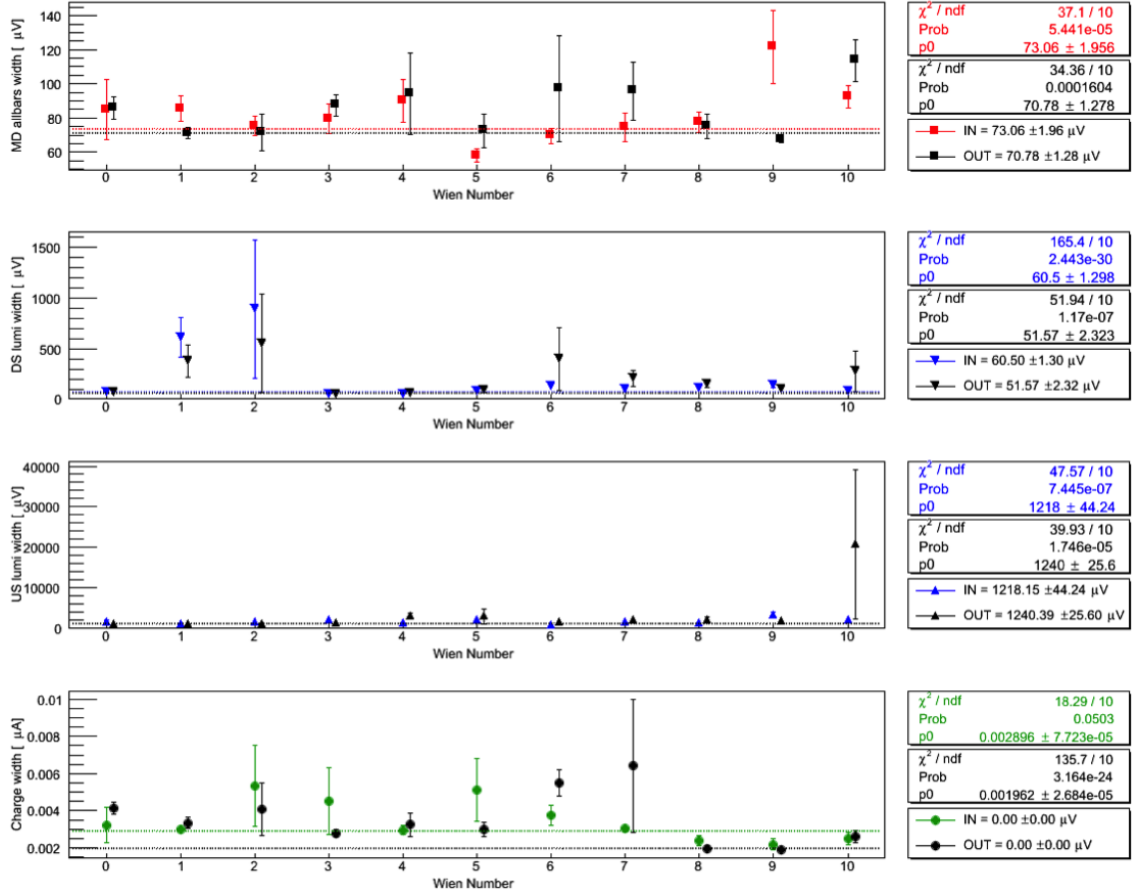


Figure 1.24 The widths of pedestal subtracted signal from Mps_Tree for MDAllbars, DSLumiSum, USLumiSum and Charge are shown.

1.5.5 Summary of Helicity Correlated Pedestal Survey

No helicity correlated pickups were seen for most of the detector channels for the entire experiment and were at $\mathcal{O}(1)$ ppb. Electronic noise levels were generally acceptable, though potentially marginal, for the USLumi channels near the end of Run 1 but improved during Run 2. The nonlinearities for MDs were extremely small. USLumi also had a nonlinearity of few percent. There is a scope for improvement in USLumi pedestal. The nonlinearity could be very large for low-yield production running on Aluminum and N → Δ but still be under 1%. Resolutions for all the detectors were reasonably stable. The helicity correlated pedestal survey results are summarized in Table 1.4.

Table 1.4 Summary of helicity correlated pedestal survey.

Channels	False Asymmetry [ppb]	Sensitivity	Nonlinearity [%]	Electronic Noise
MDAllbars	0.4	30 μ V	\ll 0.1	73 μ V
DSLumiSum	0.8	24 μ V	<1.0	61 μ V
USLumiSum	6.8	214 μ V	\sim 1.0	1240 μ V
Charge	0.2	0.0079 μ A	<0.1	0.0029 μ A

REFERENCES

- [1] T. Allison et al. The Q'weak Experimental Apparatus. 2014. (Cited on pages 2, 3, and 4.)
- [2] Josh Hoskins. *Region III rotator, beam modulation sensitivities*. PhD thesis, College of William and Mary, Williamsburg, VA, December 2014. (Cited on page 3.)
- [3] Donald Jones. *Compton polarimeter*. PhD thesis, University of Virginia, Charlottesville, VA, December 2014. (Cited on pages 3 and 11.)
- [4] Josh Hoskins. Effects of fitting BPM response with fixed phase. ELOG-Analysis-690: <https://qweak.jlab.org/elog/Analysis+&+Simulation/690>, August 2012. (Cited on page 9.)
- [5] Kent Paschke. Beam Modulation response with FFB interference. ELOG-Analysis-695: <https://qweak.jlab.org/elog/Analysis+&+Simulation/695>, August 2012. (Cited on page 10.)
- [6] Rob Mahurin. QTor misalignment estimate due to beam steering. ELOG-QTor-2: <https://qweak.jlab.org/elog/QTOR/2>, April 2011. (Cited on page 12.)
- [7] Nuruzzaman. Estimation of beam steering due to QTOR fringe field using OPTIM. ELOG-QTor-3: <https://qweak.jlab.org/elog/QTOR/3>, April 2011. (Cited on page 12.)
- [8] Jay Benesch. Private communication, 2009-2013. (Cited on page 12.)
- [9] Nuruzzaman. Low Energy Electron Deflectng Due to QTOR fringe field using OPTIM. ELOG-QTor-4: <https://qweak.jlab.org/elog/QTOR/4>, April 2011. (Cited on page 13.)
- [10] Nuruzzaman. Effect of corrector magnet in front of QTOR on beam steering due to fringe field. ELOG-QTor-5: <https://qweak.jlab.org/elog/QTOR/5>, April 2011. (Cited on page 13.)
- [11] Nuruzzaman. Effect of different fields in the corrector magnet in front of QTOR. ELOG-QTor-6: <https://qweak.jlab.org/elog/QTOR/6>, April 2011. (Cited on page 14.)
- [12] Nuruzzaman. Preliminary QTOR corrector magnet design and field map using TOSCA. ELOG-QTor-7: <https://qweak.jlab.org/elog/QTOR/7>, April 2011. (Cited on page 14.)
- [13] Nuruzzaman. Realistic QTOR corrector magnet design, field map and basics using TOSCA. ELOG-QTor-8: <https://qweak.jlab.org/elog/QTOR/8>, April 2011. (Cited on page 14.)
- [14] Nuruzzaman. Power calculation for QTOR corrector magnet. ELOG-QTor-9: <https://qweak.jlab.org/elog/QTOR/9>, April 2011. (Cited on page 14.)

- [15] Nuruzzaman. QTOR corrector magnet sensitivity to position and angle. ELOG-QTor-10: <https://qweak.jlab.org/elog/QTOR/10>, April 2011. (Cited on page 14.)
- [16] Nuruzzaman. QTOR corrector magnet field along different octant. ELOG-QTor-11: <https://qweak.jlab.org/elog/QTOR/11>, April 2011. (Cited on page 14.)
- [17] Nuruzzaman. QTOR corrector magnet project summary. ELOG-QTor-12: <https://qweak.jlab.org/elog/QTOR/12>, April 2011. (Cited on page 15.)
- [18] Buddhini Waidyawansa. *A 3% Measurement of the Beam Normal Single Spin Asymmetry in Forward Angle Elastic Electron-Proton Scattering using the Qweak Setup.* PhD thesis, Ohio University, Athens OH 45701, USA, August 2013. (Cited on pages 16 and 19.)
- [19] Buddhini Waidyawansa. Beam Position and Angle Determination in Qweak. Technical Report Qweak-DocDB-1772, December 2012. (Cited on pages 16 and 18.)
- [20] Valery Lebedev. OPTIM: Computer code for linear and non-linear optics calculations. <http://www-bdnew.fnal.gov/pbar/organizationalchart/lebedev/OptiM/optim.htm>, June 2007. (Cited on page 18.)
- [21] Nuruzzaman. Target BPM Angle Resolution from OPTIM. Q-weak Physics Meeting, Q-weak-DocDB1779: <https://qweak.jlab.org/doc-private>ShowDocument?docid=1779>, January 2013. (Cited on page 18.)
- [22] Nuruzzaman. Scheme Dependence of Rescaled Wien0 Main Detector Sensitivities. Q-weak Physics Meeting, Q-weak-DocDB1776: <https://qweak.jlab.org/doc-private>ShowDocument?docid=1776>, February 2013. (Cited on page 19.)
- [23] Nuruzzaman and *et. al.* Position and Angle Determination at the Q_{weak}^p Target for Beam Modulation. Technical Report Qweak-DocDB-1208, March 2010. Used as a reference for how the position and angle determination at the target for beam modulation in the Q_{weak}^p experiment. (Cited on page 19.)
- [24] Q weak Collaboration. The Q-weak Experiment: "A Search for New Physics at the TeV Scale via a Measurement of the Proton's Weak Charge". Technical Report E05-008 Jeopardy proposal, December 2007. (Cited on page 19.)
- [25] John Leacock. Helicity Correlated Pedestal Differences for April 2011 from Qweak Run I. Technical report, VT, VA, Nov 2011. (Cited on page 21.)

- [26] John Leacock. *Measuring the Weak Charge of the Proton and the Hadronic Parity Violation of the $N \rightarrow \Delta$ Transition.* PhD thesis, Virginia Polytechnic Institute & State University, Blacksburg, VA 24061-0002, USA, October 2012. (Cited on page 21.)